Giant magnetoresistance in helimagnets

Andrei Zadorozhnyi ●, Raz Rivlis, and Yuri Dahnovsky ●*
*Department of Physics and Astronomy/3905, 1000 E. University Avenue, University of Wyoming,
Laramie WY 82071, United States*

Magnetoresistance and ordinary Hall effects are studied depending on magnetic field, temperature, electron concentration, and the orientation between the an electric field, magnetic field, and the spin spiral propagation direction. The magnetic field is assumed to be lower than the pinning value B_{pin}. Solving the Boltzmann equation for a nonequilibrium distribution function, we find the giant magnetoresistance in helimagnets by more than one order of magnitude higher than in a ferromagnetic phase. The giant magnetoresistance is only observed along the spin spiral propagation axis with a magnetic field directed perpendicular to this axis. The explanation of this effect is given in terms of the spin separation of electrons along the spiral axis specific to a helical state. We study ordinary Hall effect and find that the Hall constant remains almost unchanged compared to the free electron model at the same electron concentration in low and high magnetic fields. We also observe the dramatic increase in anisotropy in the longitudinal conductivity with an applied magnetic field. The temperature dependence reveals the increase or decrease of magnetoresistance depending on electron concentration. We provide the explanations of the found effects using the simple models.

I. INTRODUCTION

Helimagnets are a class of materials with the unique magnetic structure called a spin spiral. In recent years, there has been growing interest in understanding the properties of spin spirals and their potential applications in spintronics [1–4]. Helimagnetism is related to skyrmions because they originate from the same interactions as spin spirals at different temperatures and magnetic fields [5]. It is known from both theoretical and experimental studies that the direction of a spin spiral in the absence of a magnetic field is defined by crystal symmetry. For example, it is a (111) direction in cubic MnSi crystals [6–11]. In the presence of a magnetic field, there are two possibilities: (a) the spiral propagation direction is still pinned to the crystal axis, and (b) the spin spiral propagates along the magnetic field and becomes conical, i.e., it acquires a nonzero net magnetic moment. Case (a) is observed when an applied external magnetic field is below the pinning value B_{pin} which is defined by material, temperature, and the direction of a magnetic field with respect to crystal axes, and case (b) corresponds to magnetic fields with $B > B_{pin}$ [6,12–18].

Helimagnetism can be caused by antisymmetric exchange [19–22], frustrated magnetism [23], and RKKY/Kondo effects [24–27]. In the previous theoretical and experimental investigations the origin of spin spirals was discussed [28–33]. The charge transport in helimagnets was experimentally investigated for $FeGe_2$ [34,35], $Fe_{1-y}Co_yGe$ [36], MnSi [37–40], Cu_2OSeO_3 [41], $SrRuO_3$ [42], and for MnP it was shown that the helicity can be controlled by electric current [1]. Thus, it is important to provide a systematic approach where these experimental data can be explained.

To study megnetotransport in helimagnets, we use the approach based on the kinetic Boltzmann equation for a nonequilibrium distribution function. In the previous research we employed the Boltzmann equation methodology to investigate the anisotropy in the longitudinal conductivity originated from the band structure distortion due to the helical and conical spin spirals. We found how it depends on Fermi energy. We also described the resistivity behavior at the phase transition from spin spiral to paramagnetic or ferromagnetic phases [43,44]. In this research, we focus only on helical structures. We assume B_{pin} to be high enough to study electron transport properties in a broad range of magnetic fields (up to 10 T). To investigate a temperature dependence of Hall effect and magnetoresistance, we require a spin-spiral phase to exist up to 90 K. It is important to emphasize that we only consider helical magnetic phase without conical component. For example, in MnP $B_{pin} = 0$ and the magnetic phase becomes conical at any nonzero magnetic field and the proposed theory becomes inapplicable [1,45].

To describe the transport properties in 3D conical magnetic materials, we consider the following Hamiltonian [46]

$$\hat{H}_0 = \hat{H}_{crys} + \hat{H}_{hel} = \frac{\hbar^2 k^2}{2m} - JS_0\hat{\boldsymbol{\sigma}} \times \boldsymbol{n}(\boldsymbol{r})$$

$$= \frac{\hbar^2 k^2}{2m} - JS(\sigma_x \cos(\varkappa z) + \sigma_y \sin(\varkappa z)), \qquad (1)$$

where J is an exchange integral between the conduction electrons and localized magnetic moments $\boldsymbol{S}$. Here $\boldsymbol{\sigma}$ is the vector of the three Pauli matrices. The spiral period of the localized spin rotation about the z axis is $L = 2\pi/\varkappa$. We organize this work as follows. In Sec. II we introduce the theoretical approach to transport properties based on the Boltzmann equation which is solved numerically using the

*yurid@uwyo.edu

original method based on the elimination of the derivative of the distribution function. In Sec. III we present the results of the calculations of magnetoresistance, ordinary Hall effect and anisotropy in the longitudinal conductivity depending on a magnetic field, temperature, electron density, and orientation between an electric field, magnetic field, and helicity propagation direction. The qualitative explanations are also provided.

II. THEORETICAL AND COMPUTATIONAL APPROACHES

Hamiltonian Eq. (1) can be exactly diagonalized where the energy bands have the following form [44]:

$$\varepsilon_{1,2} = \frac{\varepsilon_0\left(\bm{k} + \bm{e}_z\frac{\varkappa}{2}\right) + \varepsilon_0\left(\bm{k} - \bm{e}_z\frac{\varkappa}{2}\right)}{2} \pm \sqrt{J^2 S^2 + D^2}. \quad (2)$$

Here $\varepsilon_0(\bm{k})$ is an unperturbed energy band and $D = [\varepsilon_0(\bm{k} + \bm{e}_z\frac{\varkappa}{2}) - \varepsilon_0(\bm{k} - \bm{e}_z\frac{\varkappa}{2})]/2$. The eigenfunctions are expressed as follows:

$$\begin{pmatrix} \Psi_{\bm{k}}^{\uparrow(\nu)}(\bm{r}) \\ \Psi_{\bm{k}}^{\downarrow(\nu)}(\bm{r}) \end{pmatrix} = \begin{pmatrix} a_\nu(\bm{k})e^{-i\frac{\varkappa}{2}z} \\ b_\nu(\bm{k})e^{+i\frac{\varkappa}{2}z} \end{pmatrix} \psi_{0\bm{k}}(\bm{r}), \quad (3)$$

where $\psi_{0\bm{k}}$ is an unperturbed wavefunction, $\nu = 1, 2$ is a band index, and a_ν and b_ν are coefficients for spin-up and spin-down contributions to the eigenstate

$$b_2 = a_1 = \cos\frac{X}{2}, \quad b_1 = -a_2 = \sin\frac{X}{2},$$

$$\cos X = \frac{D}{\sqrt{J^2 S^2 + D^2}}. \quad (4)$$

For the transport calculations we employ the Boltzmann equation with the relaxation rate due to electron-acoustic phonon interaction [43,44]

$$-\frac{e}{\hbar}(\bm{E} + [\bm{v}^\nu \times \bm{B}])\nabla_{\bm{k}}\big(f_0(\varepsilon_\nu(\bm{k})) + f_1^\nu(\bm{k})\big)$$

$$= \sum_{\nu'}\sum_{\bm{k}'}\big(W_{\bm{k}\bm{k}'}^{\nu\nu'}f_1^{\nu'}(\bm{k}') - W_{\bm{k}'\bm{k}}^{\nu'\nu}f_1^\nu(\bm{k})\big). \quad (5)$$

Here f_0 is the equilibrium Fermi distribution function, f_1 is the nonequilibrium part of the total distribution function, $\bm{E}$ is an applied electric field, $\bm{B}$ is an applied magnetic field, $\bm{v}$ is an electron velocity, and $\nabla_{\bm{k}}$ is the gradient with respect to the wavevector. The relative directions between the electric field, magnetic field, and spin spiral axis are schematically shown in Fig. 1.

The transition rates $W_{\bm{k}\bm{k}'}^{\nu\nu'}$ are defined as follows:

$$W_{\bm{k}\bm{k}'}^{\nu\nu'} = (2\pi/\hbar)\big|\langle\bm{k}', \nu', N_{\bm{q}j}'|\Delta V|\bm{k}, \nu, N_{\bm{q}j}\rangle\big|^2 \delta(\varepsilon_\nu(\bm{k}) - \varepsilon_{\nu'}(\bm{k}')). \quad (6)$$

In this equation, ΔV is the electron-acoustic phonon interaction potential. $N_{\bm{q}j}$ is the population number of phonons with the wavevector $\bm{q}$ and the branch j determined from the Bose distribution function

$$N_{\bm{q}j} = \frac{1}{e^{\frac{\varepsilon_{ph}}{k_B T}} - 1}. \quad (7)$$

Index ν denotes an energy band number ($\nu = 1, 2$). As soon as the transition rates are found and Boltzmann equation [Eq. (5)] is solved, we can determine the electric current
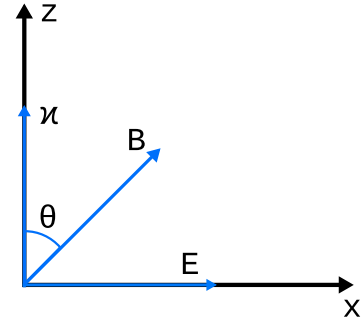

FIG. 1. Directions between the electric field $\bm{E}$, magnetic field $\bm{B}$, and spin spiral axis $\varkappa$.

density

$$j_i^\nu = e\frac{1}{(2\pi)^3}\int f_1^\nu v_i^\nu d^3k, \quad (8)$$

where v_i^ν is a velocity projection ($i = x, y, z$) determined as $v_i^\nu = \partial\varepsilon^\nu(\bm{k})/\hbar\partial k_i$.

To solve the Boltzmann equation [Eq. (5)], we have expanded it to the lowest order of f_1

$$-e\frac{\partial f_0}{\partial\varepsilon}\bm{E} \times \bm{v}^\nu - \frac{e}{\hbar}[\bm{v}^\nu \times \bm{B}] \times \big(\nabla_{\bm{k}}f_1^\nu(\bm{k})\big)$$

$$= \sum_{\nu'}\int\big(W_{\bm{k}\bm{k}'}^{\nu\nu'}f_1^{\nu'}(\bm{k}') - W_{\bm{k}'\bm{k}}^{\nu'\nu}f_1^\nu(\bm{k})\big)\frac{d^3k'}{(2\pi)^3}. \quad (9)$$

Equation (9) is a linear integrodifferential matrix equation for f_1. For numerical purposes it is important to eliminate the derivative $\nabla_{\bm{k}}f_1^\nu$. Thus, we multiply left- and right-hand sides of Eq. (9) by both the delta function of energy $\delta(\varepsilon(\bm{k}) - \varepsilon_0)$, and some differentiable function $g_n(\bm{k}, \nu)$, which will be defined below. We then integrate the equation over $\bm{k}$. The gradient term on the left-hand side can be transformed using the integration by parts resulting in the following integral form of the Boltzmann equation

$$\sum_\nu\int f_1^\nu(\bm{k})K(\bm{k}, \nu)\frac{d^3k}{(2\pi)^3}$$

$$= -\sum_\nu\int \delta(\varepsilon^\nu(\bm{k}) - \varepsilon_0)g_n(\bm{k}, \nu)\frac{\partial f_0}{\partial\varepsilon^\nu(\bm{k})}\bm{E} \times \bm{v}^\nu\frac{d^3k}{(2\pi)^3}, \quad (10)$$

where the kernel $K(\bm{k}, \nu)$ is defined as follows:

$$K(\bm{k}, \nu) = \frac{e}{\hbar}\delta(\varepsilon^\nu(\bm{k}) - \varepsilon_0)[\bm{v}^\nu \times \bm{B}] \times \nabla_{\bm{k}}g_n(\bm{k}, \nu)$$

$$+ \frac{2\pi}{\hbar}\sum_{\nu'}\int|V_{\bm{k}'\bm{k}}^{\nu'\nu}|^2\delta(\varepsilon^\nu(\bm{k}) - \varepsilon_0)\delta(\varepsilon^{\nu'}(\bm{k}') - \varepsilon_0)$$

$$\times (g_n(\bm{k}', \nu') - g_n(\bm{k}, \nu))\frac{d^3k'}{(2\pi)^3}. \quad (11)$$

Here we express the transition rates $W_{\bm{k}\bm{k}'}^{\nu\nu'}$ in accordance with Eq. (6). Equation (10) is the inhomogeneous Fredholm integral equation of the first kind. We solve it numerically in piecewise-constant approximation. The set of functions $\{g_n\}$ is chosen to provide a set of N independent equations where N is the number of points to be considered on the constant energy
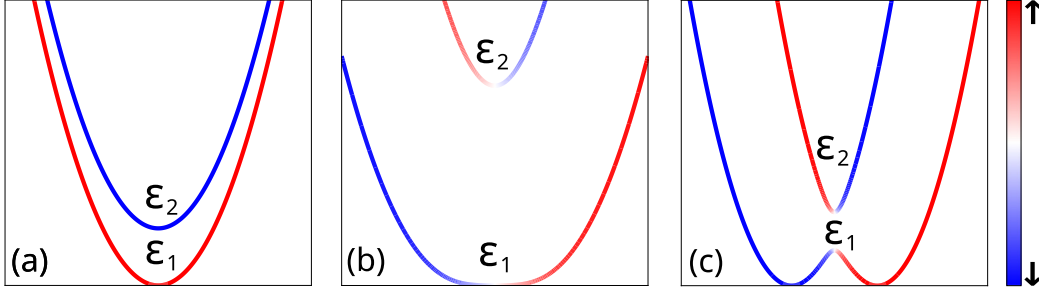
FIG. 2. Band structures for ε_1 and ε_2 for three different cases: (a) the ferromagnetic phase where $\varepsilon_{1,2}(\boldsymbol{k})$ are paraboloids, (b) a helical state where $\varepsilon_1(\boldsymbol{k})$ has one nonparabolic minimum $\hbar^2 \varkappa^2/2m < 2JS$, and (c) a helical state where $\varepsilon_1(\boldsymbol{k})$ has two symmetric minima $\hbar^2 \varkappa^2/2m > 2JS$. The blue color corresponds to the spin-$\downarrow$ projection and the red color represents the spin-$\uparrow$ projection. The mixture of the spin-up and spin-down states is shown in the middle region.

surface. To choose the functions g_n, we consider the two options: (a) $g_{r_n,\nu_n}(\boldsymbol{k}, \nu) = \delta_{\nu\nu_n} \exp\left(i\boldsymbol{r}_n \cdot \boldsymbol{k}\right)$, which is equivalent to the Fourier transform and (b) the product of the three Gaussian functions in the $\boldsymbol{k}$ space

$$g_{k_n,\nu_n}(\boldsymbol{k}, \nu) = \delta_{\nu\nu_n} g(k_x - k_{nx}) g(k_y - k_{ny}) g(k_z - k_{nz}),$$

$$g(k - k_n) = \frac{1}{\sqrt{2\pi} w} e^{-\frac{1}{2w^2}(k-k_n)^2}, \quad (12)$$

where w is the width of the Gaussian function. In the limit of $w \to 0$, Eq. (10) transforms to Eq. (9). Both sets of functions provide the same numerical results, from which we conclude that the approach employed in this paper is trustworthy. The Gaussian functions are chosen for the calculations.

To solve the Boltzmann equation [Eq. (10)], we have written original code where the relaxation rates are considered within the first Born approximation with respect to electron-acoustic phonon interaction. We have used nonparabolic $\varepsilon_1(\boldsymbol{k})$ and $\varepsilon_2(\boldsymbol{k})$ as defined in Eq. (2) for the solution of the Boltzmann equation. The numerical simulations include the calculation of a constant energy surface, which contains multiple subsurfaces. For each $(\nu, \boldsymbol{k})$ and $(\nu', \boldsymbol{k}')$ at the energy surface, the transition rates have been found. The first order correction to the distribution function has been calculated and substituted into the expression for the current [see Eq. (8)]. Then the conductivity and resistivity tensors have been computed.

For the calculations, we consider a parabolic form for unperturbed energy band $\varepsilon_0(\boldsymbol{k})$ [the first term of Hamiltonian Eq. (1)]. $\varepsilon_{1,2}(\boldsymbol{k})$ are presented in Fig. 2. As shown in Fig. 2(a), $\varepsilon_{1,2}(\boldsymbol{k})$ are symmetric paraboloids in a pure ferromagnetic state. The helical state with the single minimum in $\varepsilon_1(\boldsymbol{k})$ ($\hbar^2 \varkappa^2/2m < 2JS$ case) is depicted in Fig. 2(b). As shown in Fig. 2(c), $\varepsilon_1(\boldsymbol{k})$ has two symmetric minima in the k_z direction for a helical state $\hbar^2 \varkappa^2/2m > 2JS$. The two-minima shape of $\varepsilon_1(\boldsymbol{k})$ is a saddle rather than a Mexican-hat shape discussed in Ref. [47] for the Rashba effect. Indeed, in the x and y directions $\varepsilon_{1,2}(\boldsymbol{k})$ are still parabolas. The blue and red colors stand for spin-down and spin-up states, respectively.

III. RESULTS AND DISCUSSION

In this section we present the results of the numerical calculations using the original code described above. Here

we discuss the anisotropy in the longitudinal conductivity, the ordinary Hall effect, and the magnetoresistance. For calculations we have chosen the following values of the parameters: the spiral period $L = 2\pi/\varkappa = 3.7$ nm and the effective mass $m = 0.5 m_e$. The conductivity and the Hall constant are normalized by $\sigma_0 = 671 \, \Omega^{-1} \, \text{cm}^{-1}$ and $R_0 = 0.0015 \, \Omega \, \text{cm} \, \text{T}^{-1}$, respectively.

A. Anisotropy in the longitudinal conductivity

In Fig. 3 we present $\sigma_\perp = (\sigma_{zz} - \sigma_{xx})/2$ with respect to chemical potential at different magnetic fields. The magnetic field is aligned with the spin spiral propagation direction while $E_x = E_z$, $E_y = 0$. As shown in Fig. 3, the magnetic field substantially increases the perpendicular current value by one order of magnitude at $B = 3$ T. Indeed, the larger the magnetic field, the smaller σ_{xx}. Thus, $\sigma_\perp = (\sigma_{zz} - \sigma_{xx})/2$ increases with magnetic field. The shape of the curves in Fig. 3 was discussed in the prior work [43]. The sharp increase at $\mu = 0.1$ eV can be explained by the contribution of the upper band.
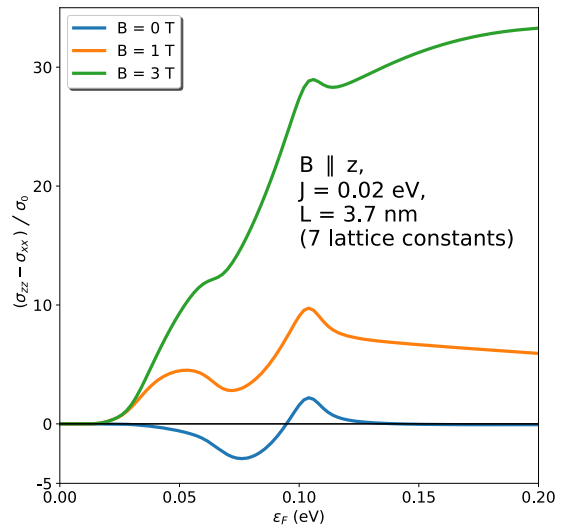

FIG. 3. Fermi energy dependence of the anisotropy in the longitudinal conductivity in the absence (the blue curve) and in the presence (the orange and green curves) of the different magnetic fields.
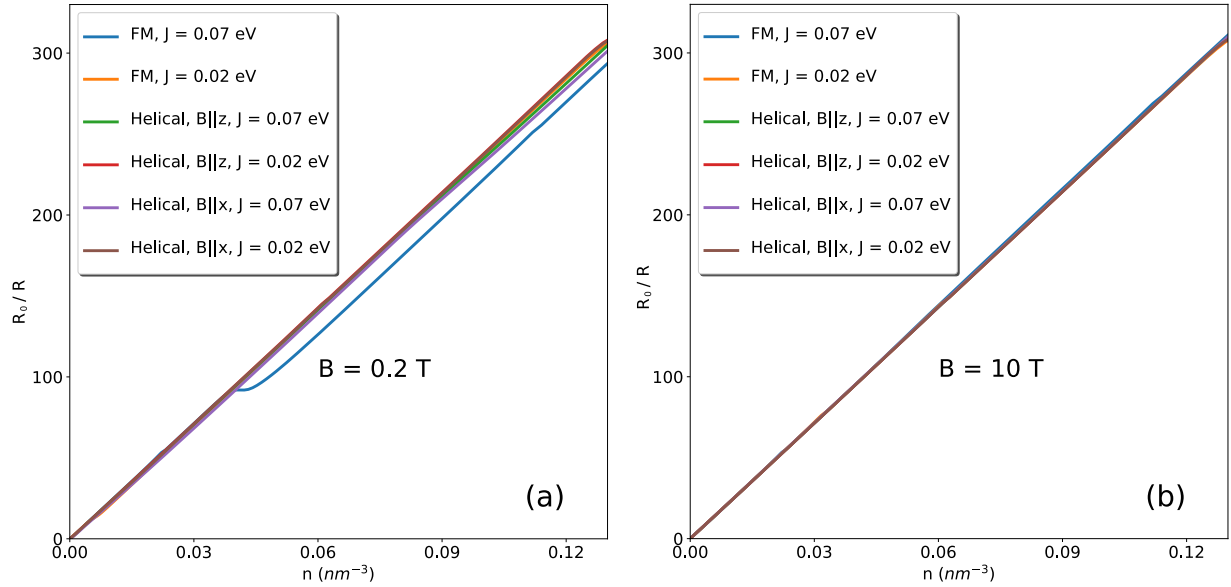
FIG. 4. Inverse ordinary Hall constant depending on the electron density for different structures: ferromagnetic (FM), helical (HM) with magnetic field along the spin spiral propagation direction, and helical with magnetic field perpendicular to the spin spiral propagation direction. The exchange integrals, $J = 0.07$ and $J = 0.02$ eV, are taken at magnetic fields (a) $B = 0.2$ T and (b) $B = 10$ T. The temperature is $T = 40$ K.

B. Hall effect

For the normal Hall effect, $\rho_{xy}(-\boldsymbol{B}) = -\rho_{xy}(\boldsymbol{B})$. The results of the calculation of the Hall constant R ($\rho_{xy} = RB$) with respect to electron concentrations are shown in Fig. 4.

In this figure we consider the following cases: the blue and orange lines stand for the ferromagnetic phase at $= 40$ K with the exchange integral $J = 0.07$ eV and $J = 0.02$ eV, respectively [see Fig. 2(a)]. The green line corresponds to the shallow double minimum ($J = 0.07$ eV) helical case with $\boldsymbol{B} \parallel z$ [see Fig. 2(b)]. The red line corresponds to sharp double-minimum ($J = 0.02$ eV) helical case with $\boldsymbol{B} \parallel z$ [see Fig. 2(c)]. The purple line represents the shallow double minimum ($J = 0.07$ eV) helical case with $\boldsymbol{B} \parallel x$ [see Fig. 2(b)]. The brown line corresponds to the sharp double-minimum ($J = 0.02$ eV) helical case with $\boldsymbol{B} \parallel x$ [see Fig. 2(c)]. As shown in Fig. 4, all cases have similar dependencies. Thus, we conclude that the two-band structure and helicity do not contribute to the Hall effect. For a free electron in high magnetic field $R \approx -1/(ecn)$, where e is the electron charge, c is the speed of light, and n is the electron density. This result remains the same in the helical case. Because the main formula for R is mass and τ independent at high magnetic fields, we would expect that in the helical case the dependencies with electron concentration remain close to those of the free electron model.

We have obtained the expression for the Hall constant in the weak field approximation $\omega_c \tau \ll 1$, where ω_c is the cyclotron frequency. In the same manner as derived in Anselm, Chap. 9, for the ferromagnetic case [see Fig. 2(a)] [48]

$$R \approx -\frac{\left(n_1 \langle \tau_1^2 \rangle + n_2 \langle \tau_2^2 \rangle\right)}{ce(n_1 \langle \tau_1 \rangle + n_2 \langle \tau_2 \rangle)^2}. \quad (13)$$

Here $n_{1,2}$ are electron densities in the spin-up and spin-down ferromagnetic states, correspondingly. $n = n_1 + n_2$. $\langle \tau_{1,2} \rangle$ are

the average relaxation times defined as follows (in the high temperature limit):

$$\langle \tau \rangle = \frac{4}{3\sqrt{\pi}} \int_0^{+\infty} \tau(x) e^{-x} x^{3/2} dx. \quad (14)$$

In the numerical calculations we use all temperatures instead of the high temperature approximation. As shown in Fig. 4(a), at the electron density corresponding to the Fermi energy close to the upper band, we find the drop in $1/R$ in the pure ferromagnetic case at low magnetic fields

$$\left(\frac{1}{R}\right)_{\text{hel}} > \left(\frac{1}{R}\right)_{FM}. \quad (15)$$

This effect can be explained from the following considerations: the contribution of the lower band is higher when the second band is included. Indeed, $\tau_{1,2} \sim \varepsilon_{1,2}^{-1/2}$ and $n_{1,2} \sim \varepsilon^{3/2}$. Hence, $1/R$ is proportional to the following expression

$$\frac{1}{R} \sim \frac{(\varepsilon_1 + \varepsilon_2)^2}{\sqrt{\varepsilon_1} + \sqrt{\varepsilon_2}}. \quad (16)$$

As shown in Fig. 2(c), the two bands can be presented as two shifted identical parabolas with the densities $n_1 = n_2 = n/2$. Hence, $(1/R)_{\text{hel}} \sim n = n_1 + n_2$. In the ferromagnetic case near the bottom of the upper band $n_1 \gg n_2$ and, therefore, $\varepsilon_1 \gg \varepsilon_2$. $(1/R)_{FM} \sim n_1 - n_1^{2/3} n_2^{1/3} < n$. Consequently, we conclude that $(1/R)_{FM}$ grows slower than n. Additionally, it is important to understand why at higher electron densities two lines in Fig. 4(a) are parallel. Indeed, if we assume $J \ll \varepsilon_{1,2}$, we provide the expansion for $\varepsilon_{1,2} = \varepsilon_0 \pm J$:

$$\left.\left(\frac{1}{R}\right)_{FM}\right|_{J \ll \varepsilon_{1,2}} \sim n\left(1 - \frac{J^2}{8\varepsilon_0^2}\right). \quad (17)$$

Thus, the main term gives the same slope and the two lines are approximately parallel. We expect them to converge at very high values of $\varepsilon_{1,2}$. As shown in Fig. 4(b), for high magnetic fields $\omega_c \tau \gg 1$, the helicity doesn't contribute to the electron density dependence of $1/R$. We find the generalization of the high field dependence of Hall constant to ferromagnetic case

$$\frac{1}{R} = -ecn = -ec(n_1 + n_2). \tag{18}$$

All the lines in Fig. 4(b) are very close to one another.

$$\frac{\Delta \rho}{\rho} = \left(\frac{Be}{mc}\right)^2 \frac{(n_1 \langle \tau_1 \rangle + n_2 \langle \tau_2 \rangle)(n_1 \langle \tau_1^3 \rangle + n_2 \langle \tau_2^3 \rangle) - (n_1 \langle \tau_1^2 \rangle + n_2 \langle \tau_2^2 \rangle)^2}{(n_1 \langle \tau_1 \rangle + n_2 \langle \tau_2 \rangle)^2}. \tag{19}$$

For strong magnetic fields the magnetoresistance is field independent in ferromagnetic state

$$\frac{\Delta \rho}{\rho} = \frac{(n_1 \langle \tau_1 \rangle + n_2 \langle \tau_2 \rangle)\left(n_1 \left\langle \frac{1}{\tau_1} \right\rangle + n_2 \left\langle \frac{1}{\tau_2} \right\rangle\right)}{(n_1 + n_2)^2} - 1. \tag{20}$$

In Fig. 5 we demonstrate the dependence of the magnetoresistance on an applied magnetic field for different temperatures in the range of $20 \, \text{K} \leqslant T \leqslant 90 \, \text{K}$. According to Eq. (19) we observe quadratic dependence of magnetoresistance for all orientations and temperatures at low fields. For higher magnetic fields we find that the magnetoresistance approaches the plateaus in accordance with Eq. (20). At high temperatures and weak magnetic fields, the temperature dependence of the relaxation rate is $\tau \sim T^{-3/2}$. Therefore, $\Delta \rho / \rho \sim T^{-3}$. The higher the temperature, the lower the magnetoresistance is at low fields. At low and medium temperatures the plateau value at high fields is temperature dependent [49].

In Fig. 6 we present the magnetoresistance depending on an applied magnetic field at very low electron concentrations where ε_F is close to the bottom of the lower band in the shallow double minimum case. Because of the high electron effective mass in the z direction the low magnetic field range is extended to higher magnetic fields [see Eq. (20)], and therefore, we do not observe the plateaus in the magnetoresistance in Fig. 6(c). In the x and y directions the effective masses are lower than in the z directions and the weak magnetic field range is shorter, and we can observe the plateaus for low temperatures as shown in Figs. 6(a) and 6(b). The giant magnetoresistance is found in Fig. 6(c) where the magnetic field is applied along the x axis and the magnetoresistance is calculated along the spin spiral propagation direction, z axis. The magnetic field diverts the electrons clockwise as shown in Fig. 7. However, k_z must be always positive for spin-up electrons and negative for spin-down electrons. The transitions from $k_z > 0$ to $k_z < 0$ and vice versa are forbidden by the spin conservation. Therefore, the magnetic field can rotate the electrons to the point where $k_z \approx 0$ as shown in Fig. 7, therefore depleting the concentration of electrons moving in the z direction.

C. Magnetoresistance

In this subsection we study the magnetoresistance depending on the magnetic field, electron density, temperature, and the angles between the electric field, magnetic field, and helicity propagation vector. We show that these dependencies are more dramatic than the Hall effect. Before describing the results of the calculations, we present a theory for a magnetoresistance in a ferromagnet in weak ($\omega_c \tau \ll 1$) and strong ($\omega_c \tau \gg 1$) magnetic fields. We generalize the derivation presented in the book of Anselm, Chap. 9 [48].

For weak magnetic fields in ferromagnetic state (no helicity)

Thus, the magnetoresistance in the z direction becomes much higher.

In Fig. 8 the concentration of electrons is such that the Fermi energy is slightly above the maximum of the lower band as shown in the insertion of Fig. 8(a). In Figs. 8(a) and 8(b) the low field range exhibiting the parabolic behavior is very narrow. In the intermediate and higher fields the $\Delta \rho / \rho$ almost reaches the plateaus. According to Askerov [49], the lower the temperature, the lower the plateau value is. However, in Fig. 8(c) the dependence is reversed. Moreover, the value of magnetoresistance is one order of magnitude higher than those of presented in Figs. 8(a) and 8(b). The inverse temperature dependence can be explained by the depletion of electrons moving in the z direction. The forbidden transition from the spin-up to the spin-down state, i.e., from $k_z > 0$ to $k_z < 0$, and vice versa, can be allowed due to the electron-phonon scattering. This probability increases with temperature. The higher the scattering probability, the lower magnetoresistance in the z direction is.

In Fig. 9 we present the dependence of magnetoresistance with electron density for $B = 10$ T at $T = 40$ K and $J = 0.07$ eV that corresponds to the shallow double minimum lower band in helimagnetic phase [see Fig. 2(b)]. The blue line represents the ferromagnetic structure. The bands are shown in Fig. 2(a). The orange curve describes the magnetoresistance along the x axis with magnetic field applied along the z axis in the helimagnetic phase. The green and red curves stand for magnetoresistance along y and z axes, respectively, with magnetic field applied along the x axis. At low concentrations, i.e., small chemical potentials, there is the high temperature limit for all cases shown in Fig. 9. Therefore, the magnetoresistance is high [49]. The magnetoresistance drops with chemical potential below the minimum of the upper band. To explain such a drop, we consider the ferromagnetic case. We use Eq. (20) where $n_2 = 0$ (no upper band). At low temperatures the average $\langle \tau \rangle = \tau(\varepsilon_F)$ and $\langle 1/\tau \rangle = 1/\tau(\varepsilon_F)$. Then it is easy to show that $\Delta \rho / \rho = 0$. When ε_F reaches the bottom of the upper band, there is the high temperature limit in averages for $\langle \tau_2 \rangle$ and therefore, the magnetoresistance increases. When the concentration of electrons is high enough, the high temperature limit turns into a low temperature one
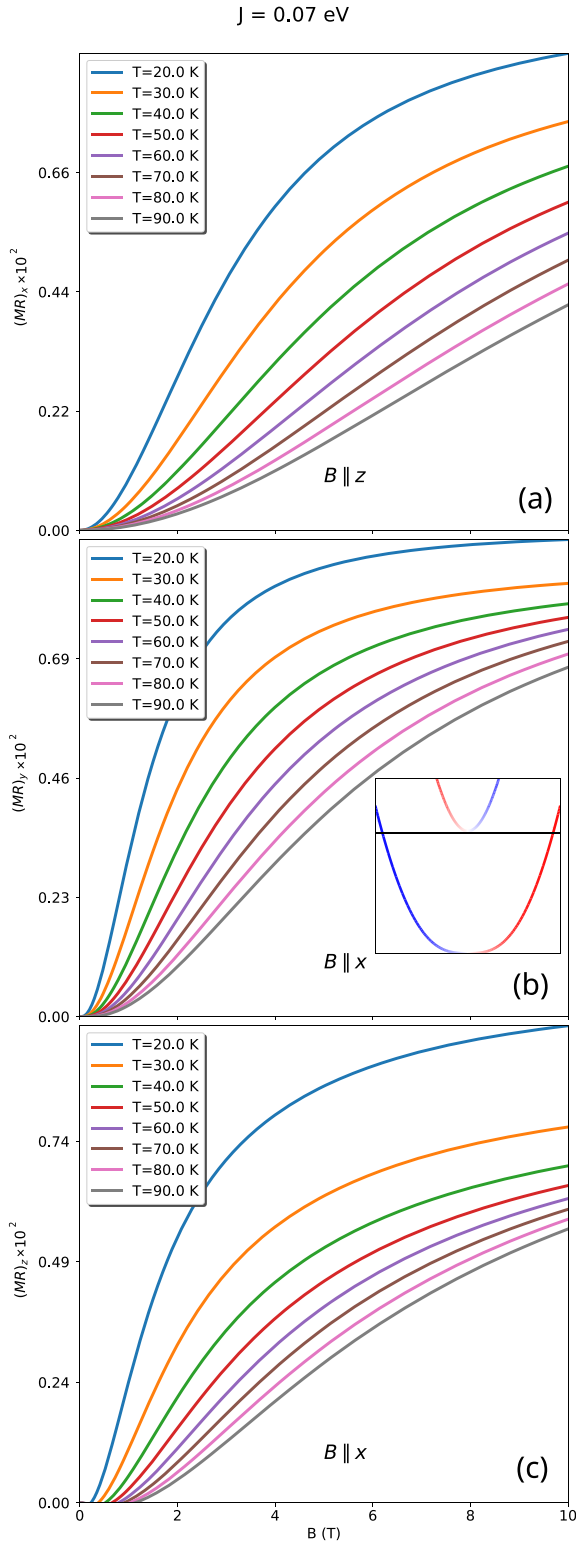
FIG. 5. Magnetic field dependence of the magnetoresistance in helical structures at different temperatures (a) in the x direction where the magnetic field is applied along the z axis (spin spiral propagation direction), (b) in the y direction where the magnetic field is applied along the x axis, and (c) in the y direction where the magnetic field is applied along the x axis. $J = 0.07$ eV and the Fermi energy is taken near the bottom of the upper energy band shown in the insertion.
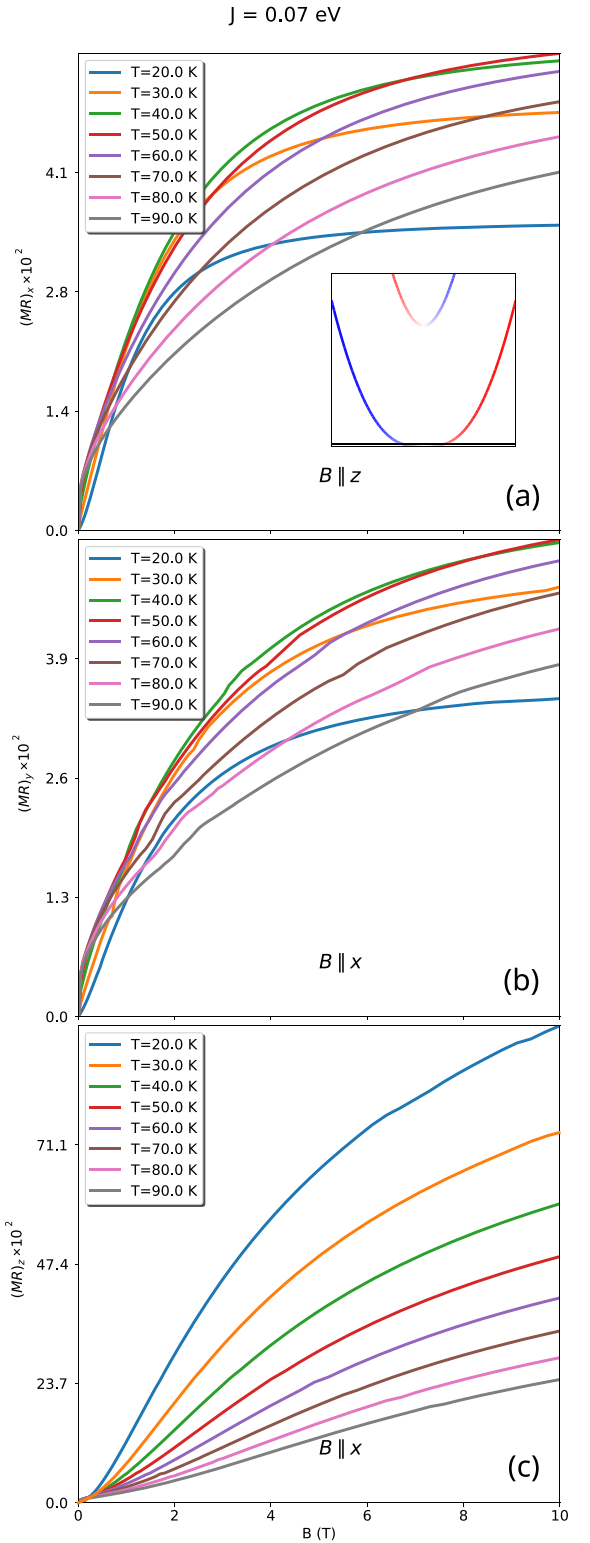
FIG. 6. Magnetic field dependence of the magnetoresistance in helical structures at different temperatures (a) in the x direction where the magnetic field is applied along the z axis (spin spiral propagation direction), (b) in the y direction where the magnetic field is applied along the x axis, and (c) in the y direction where the magnetic field is applied along the x axis. $J = 0.07$ eV and the Fermi energy is taken near the bottom of the lower energy band shown in the insertion.
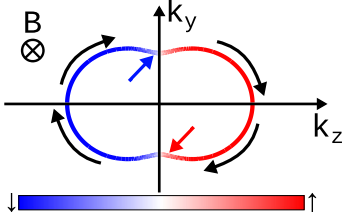
FIG. 7. Constant energy cross-section taken at the bottom of the lower band. The magnetic field is directed inward. The black arrows indicate the direction of the electron motion due to the magnetic field. The red and blue colors correspond to spin-up and spin-down electrons, respectively. The blue and red arrows indicate the regions of accumulation of the electrons at $k_z \approx 0$.

and the magnetoresistance becomes

$$\frac{\Delta \rho}{\rho}\bigg|_{\text{highfield}} = \frac{n_1 n_2}{(n_1 + n_2)^2}\left(\frac{\tau_1}{\tau_2} + \frac{\tau_2}{\tau_1} - 2\right). \quad (21)$$

At very large electron concentration $\tau_1 \approx \tau_2$ and $\Delta\rho/\rho = 0$. When the helicity is included, the curves do not exhibit the peak in the magnetoresistance at higher concentrations. Indeed, at high chemical potentials, $\varepsilon(\mathbf{k})$ can be represented by two parabolas shown in Figs. 2(b) and 2(c). In this case there is no gap between them, and therefore, the peak from the second band is not observable. Another important feature is huge magnetoresistance described by the red curve in Fig. 9. Such an increase can be explained from the considerations based on Fig. 7. As discussed above, the electrons are rotated by the magnetic field in the yz plane and tend to accumulate at $k_z \approx 0$. Thus, the concentration of electrons in the z direction is depleted and the magnetoresistance in the z direction increases compared to that of calculated in the y direction.

In Fig. 10 we describe the magnetoresistance when $B = 10$ T, $T = 40$ K, and $J = 0.02$ eV corresponding to the two minima band structure for the lower band in helical phase as shown in Fig. 2(c). If we compare the dependencies presented in Fig. 10 with that of presented in Fig. 9, we find the new qualitative feature, the zero values in the red curve in range of concentration $0.005 < n < 0.01$. The peak in the red curve is located between the maximum if the lower band and minimum of the upper one. The rest of the curves exhibit the similar dependencies. To explain the existence of the low values of magnetoresistance for the red curve, we use the following consideration: if the Fermi energy is lower than the maximum of the lower band, there are two temperature limits, the high temperature limit (low electron concentration) and the low temperature limit (high electron concentrations). The former exhibits the peak in magnetoresistance, the latter demonstrates the vanishing values. Then, if the chemical potential is above the maximum of the lower band, we find the increase in the magnetoresistance. Such an increase can be explained in terms of the considerations described by Fig. 7.

IV. CONCLUSIONS

In this work we have studied magnetoresistance and Hall effect at different temperatures, electric concentrations, and
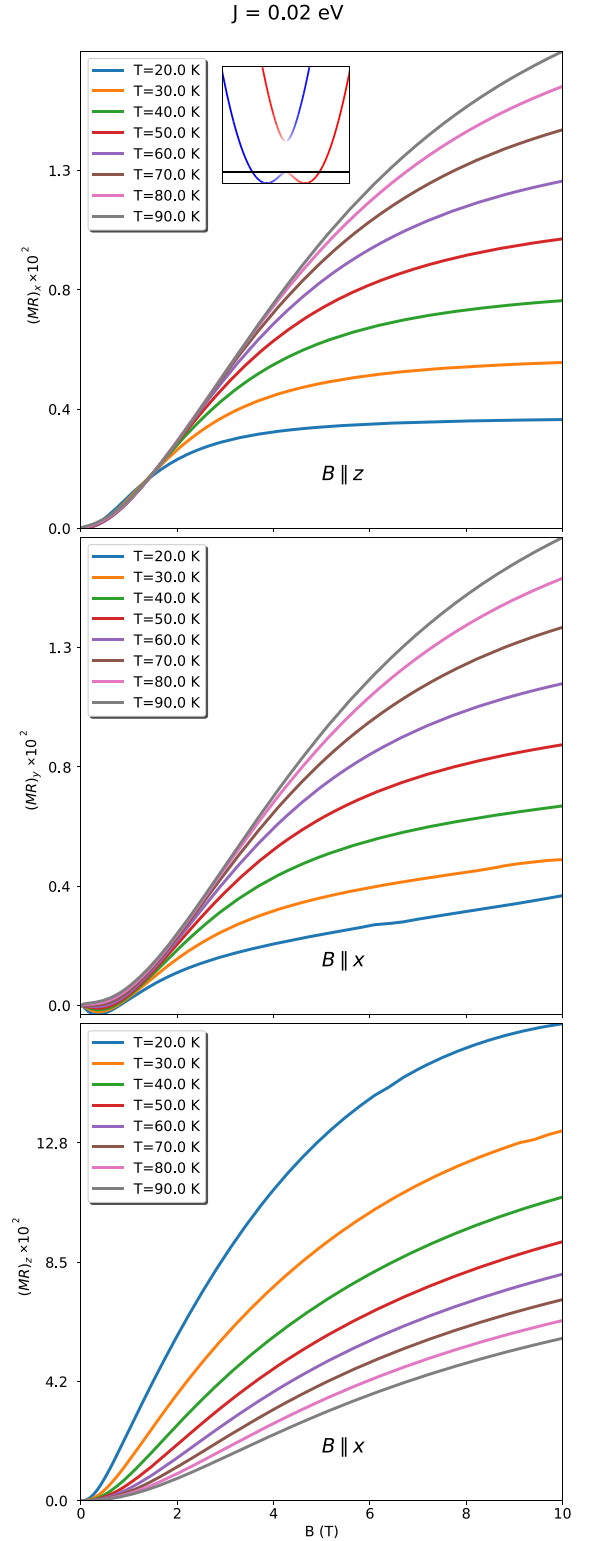

FIG. 8. Magnetic field dependence of the magnetoresistance in helical structures at different temperatures (a) in the x direction where the magnetic field is applied along the z axis (spin spiral propagation direction), (b) in the y direction where the magnetic field is applied along the x axis, and (c) in the y direction where the magnetic field is applied along the x axis. $J = 0.02$ eV and the Fermi energy is taken near the peak of the lower energy band shown in the insertion.
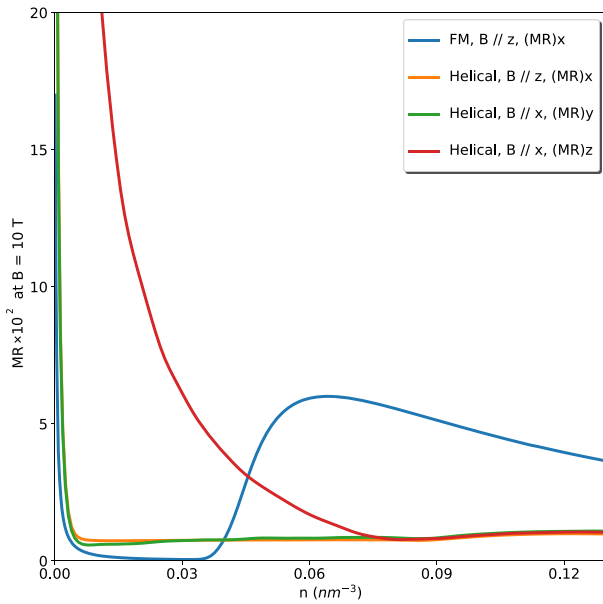
FIG. 9. Electron concentration dependence of the magnetoresistance at magnetic field $B = 10$ T and temperature $T = 40$ K for $J = 0.07$ eV. The red line represents the ferromagnetic case, the blue line corresponds the helical spiral with $\boldsymbol{B}$ along the spin spiral propagation direction, the orange line stands for the spin spiral with $\boldsymbol{B}$ along the x axis perpendicular to the spin spiral propagation direction, calculated along the y direction and the green curve represents the helical state with $\boldsymbol{B}$ along the x axis calculated along the z axis, i.e., the spin spiral propagation direction.

magnetic fields in helimagnets solving the Boltzmann equation in the presence of electric and magnetic fields. For relaxation, we have considered the electron-acoustic phonon interaction. To solve the equation we have written original code.

We have found that anisotropy in the longitudinal conductivity $\sigma_{zz} - \sigma_{xx}$ drastically increases with the magnetic field along the z axis because of the decrease of σ_{xx} matrix element.

We have calculated how $1/R$ depends on n for different field geometry in helimagnets and compared the results with the free electron model for high and low magnetic fields. We have found almost no differences for all cases. However, there is the feature at low magnetic fields where the inverse Hall constant is slightly below for the ferromagnetic case for electron concentrations corresponding to the bottom of the upper energy band. We have explained this deviation using Eq. (13).
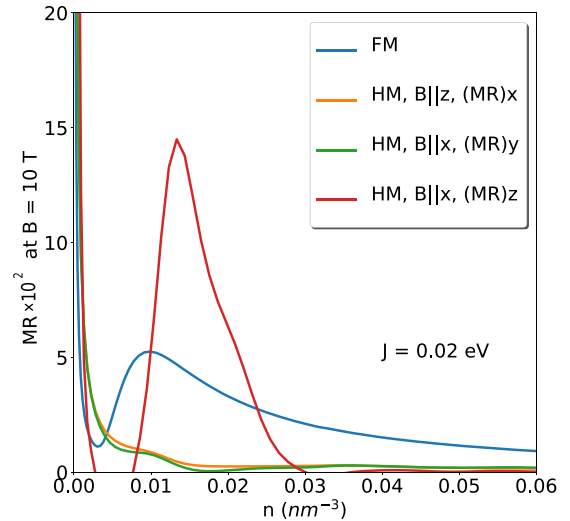

FIG. 10. Electron concentration dependence of the magnetoresistance at magnetic field $B = 10$ T and temperature $T = 40$ K for $J = 0.02$ eV. The red line represents the ferromagnetic case, the blue line corresponds the helical spiral with $\boldsymbol{B}$ along the spin spiral propagation direction, the orange line stands for the spin spiral with $\boldsymbol{B}$ along the x axis perpendicular to the spin spiral propagation direction, calculated along the y direction and the green curve represents the helical state with $\boldsymbol{B}$ along the x axis calculated along the z axis, i.e., the spin spiral propagation direction.

The more dramatic effects occur in magnetoresistance. We have found the giant magnetoresistance (more than one order of magnitude higher than that of the ferromagnet) in the spin spiral propagation direction, the z axis, when the magnetic field is applied perpendicular to it. There is a special feature of helimagnets when the bands are spin separated in the k_z direction. This property allows the electron concentration to be depleted in the k_z direction increasing the magnetoresistance (see Fig. 7). In high magnetic fields we observe the dramatic behavior of magnetoresistance with concentration (see Fig. 10) and found that the giant magnetoresistance exists only in the specific range of electron concentrations.

[1] N. Jiang, Y. Nii, H. Arisawa, E. Saitoh, and Y. Onose, Nat. Commun. **11**, 1601 (2020).

[2] N. Mohanta, S. Okamoto, and E. Dagotto, Phys. Rev. B **102**, 064430 (2020).

[3] V. V. Ustinov and I. A. Yasyulevich, Phys. Rev. B **102**, 134431 (2020).

[4] Y. Goto, H. Ishihara, and N. Yokoshi, Jpn. J. Appl. Phys. **60**, 098001 (2021).

[5] L. J. Bannenberg, R. Sadykov, R. M. Dalgliesh, C. Goodway, D. L. Schlagel, T. A. Lograsso, P. Falus, E. Lelièvre-Berna, A. O. Leonov, and C. Pappas, Phys. Rev. B **100**, 054447 (2019).

[6] O. Nakanishi, A. Yanase, A. Hasegawa, and M. Kataoka, Solid State Commun. **35**, 995 (1980).

[7] P. Bak and M. H. Jensen, J. Phys. C **13**, L881 (1980).

[8] S. V. Grigoriev, A. S. Sukhanov, and S. V. Maleyev, Phys. Rev. B **91**, 224429 (2015).

[9] Y. Ishikawa, K. Tajima, D. Bloch, and M. Roth, Solid State Commun. **19**, 525 (1976).

[10] M. L. Plumer and M. B. Walker, J. Phys. C **14**, 4689 (1981).

[11] S. V. Grigoriev, S. V. Maleyev, A. I. Okorokov, Y. O. Chetverikov, and H. Eckerlebe, Phys. Rev. B **73**, 224440 (2006).

[12] S. V. Maleyev, Phys. Rev. B **73**, 174402 (2006).

[13] S. V. Grigoriev, S.-A. Siegfried, E. V. Altynbayev, N. M. Potapova, V. Dyadkin, E. V. Moskvin, D. Menzel, A. Heinemann, S. N. Axenov, L. N. Fomicheva *et al.*, Phys. Rev. B **90**, 174414 (2014).

[14] O. Nakanishi, M. Kataoka, and A. Yanase, J. Magn. Magn. Mater. **31-34**, 339 (1983).

[15] N. I. Kulikov and V. V. Tugushev, Sov. Phys. Uspekhi **27**, 954 (1984).

[16] M. L. Plumer, J. Phys.: Condens. Matter **2**, 7503 (1990).

[17] C. Pfleiderer, D. Reznik, L. Pintschovius, and H. Löhneysen, Phys. B: Condens. Matter **359-361**, 1159 (2005).

[18] L. Schmidt, J. Hagemeister, P.-J. Hsu, A. Kubetzka, K. von Bergmann, and R. Wiesendanger, New J. Phys. **18**, 075007 (2016).

[19] J. Inoue and S. Maekawa, Phys. Rev. Lett. **74**, 3407 (1995).

[20] J. Xiao, A. Zangwill, and M. D. Stiles, Phys. Rev. B **73**, 054428 (2006).

[21] O. V. Yazyev and M. I. Katsnelson, Phys. Rev. Lett. **100**, 047209 (2008).

[22] L. D. Landau and E. M. Lifshitz, *Electrodynamics of Continuous Media* (Pergamon, New York, 1984).

[23] A. S. Sukhanov, Y. V. Tymoshenko, A. A. Kulbakov, A. S. Cameron, V. Kocsis, H. C. Walker, A. Ivanov, J. T. Park, V. Pomjakushin, S. E. Nikitin *et al.*, Phys. Rev. B **105**, 134424 (2022).

[24] Z. Wang, Y. Su, S.-Z. Lin, and C. D. Batista, Phys. Rev. Lett. **124**, 207201 (2020).

[25] R. Ozawa, S. Hayami, and Y. Motome, Phys. Rev. Lett. **118**, 147205 (2017).

[26] S. Hayami, R. Ozawa, and Y. Motome, Phys. Rev. B **95**, 224424 (2017).

[27] S. Hayami and Y. Motome, Phys. Rev. B **103**, 024439 (2021).

[28] M. Bornemann, S. Grytsiuk, P. F. Baumeister, M. dos Santos Dias, R. Zeller, S. Lounis, and S. Blügel, J. Phys.: Condens. Matter **31**, 485801 (2019).

[29] M. Deutsch, O. L. Makarova, T. C. Hansen, M. T. Fernandez-Diaz, V. A. Sidorov, A. V. Tsvyashchenko, L. N. Fomicheva, F. Porcher, S. Petit, K. Koepernik *et al.*, Phys. Rev. B **89**, 180407(R) (2014).

[30] A. O. Leonov and C. Pappas, Front. Phys. **11**, 1105784 (2023).

[31] B. Ding, J. Liu, H. Li, J. Liang, J. Chen, Z. Li, X. Li, X. Xi, Z. Cheng, J. Wang *et al.*, Adv. Funct. Mater. **32**, 2200356 (2022).

[32] Y. Kato, S. Hayami, and Y. Motome, Phys. Rev. B **104**, 224405 (2021).

[33] F. N. Rybakov, A. B. Borisov, S. Blügel, and N. S. Kiselev, New J. Phys. **18**, 045002 (2016).

[34] S. Tang, B. Chen, Y. Huang, X. Zeng, and Y. Yao, AIP Adv. **8**, 065220 (2018).

[35] C. P. Adams, T. E. Mason, S. A. M. Mentink, and E. Fawcett, J. Phys.: Condens. Matter **9**, 1347 (1997).

[36] C. S. Spencer, J. Gayles, N. A. Porter, S. Sugimoto, Z. Aslam, C. J. Kinane, T. R. Charlton, F. Freimuth, S. Chadov, S. Langridge *et al.*, Phys. Rev. B **97**, 214406 (2018).

[37] T. Yokouchi, N. Kanazawa, A. Kikkawa, D. Morikawa, K. Shibata, T. Arima, Y. Taguchi, F. Kagawa, and Y. Tokura, Nat. Commun. **8**, 866 (2017).

[38] R. Ritz, M. Halder, C. Franz, A. Bauer, M. Wagner, R. Bamler, A. Rosch, and C. Pfleiderer, Phys. Rev. B **87**, 134424 (2013).

[39] V. V. Glushkov, I. I. Lobanova, V. Y. Ivanov, and S. V. Demishev, JETP Lett. **101**, 459 (2015).

[40] A. Neubauer, C. Pfleiderer, B. Binz, A. Rosch, R. Ritz, P. G. Niklowitz, and P. Böni, Phys. Rev. Lett. **102**, 186602 (2009).

[41] A. Aqeel, M. Azhar, N. Vlietstra, A. Pozzi, J. Sahliger, H. Huebl, T. T. M. Palstra, C. H. Back, and M. Mostovoy, Phys. Rev. B **103**, L100410 (2021).

[42] S. D. Seddon, D. E. Dogaru, S. J. R. Holt, D. Rusu, J. J. P. Peters, A. M. Sanchez, and M. Alexe, Nat. Commun. **12**, 2007 (2021).

[43] A. Zadorozhnyi and Y. Dahnovsky, J. Phys.: Condens. Matter **35**, 015701 (2022).

[44] A. Zadorozhnyi and Y. Dahnovsky, Phys. Rev. B **107**, 035202 (2023).

[45] A. Takase and T. Kasuya, J. Phys. Soc. Jpn. **49**, 489 (1980).

[46] P. Kurz, F. Förster, L. Nordström, G. Bihlmayer, and S. Blügel, Phys. Rev. B **69**, 024415 (2004).

[47] A. Zadorozhnyi and Y. Dahnovsky, Phys. Rev. B **105**, 014445 (2022).

[48] A. Anselm, *Introduction to Semiconductor Theory* (Mir, Moscow, 1981).

[49] B. Askerov, *Kinetic Effects in Semiconductors (in Russian)* (Nauka, Leningrad, 1970).